

# Coherent all-optical control of a solid-state spin via a double $\Lambda$ -system

C. Adambukulam,<sup>1,\*</sup> J. A. Scott,<sup>2,3</sup> S. Q. Lim,<sup>4</sup> I. Aharonovich,<sup>2,5</sup> A. Morello,<sup>1</sup> and A. Laucht<sup>1,†</sup>

<sup>1</sup>*School of Electrical Engineering and Telecommunications,  
University of New South Wales, Kensington NSW 2052, Australia*

<sup>2</sup>*School of Mathematical and Physical Sciences, University of Technology Sydney, Ultimo NSW 2007, Australia*

<sup>3</sup>*The University of Sydney Nano Institute, The University of Sydney, Camperdown NSW 2006, Australia*

<sup>4</sup>*Centre of Excellence for Quantum Computation and Communication Technology,  
School of Physics, University of Melbourne, Melbourne VIC 3010, Australia*

<sup>5</sup>*ARC Centre of Excellence for Transformative Meta-Optical Systems (TMOS),  
Faculty of Science, University of Technology Sydney, Ultimo NSW 2007, Australia*

(Dated: February 6, 2024)

All-optical control enables fast quantum operations on color center spins that are typically realized via a single Raman transition in a  $\Lambda$ -system. Here, we simultaneously drive both Raman transitions in a double  $\Lambda$ -system to control the spin of a germanium vacancy (GeV) in diamond. In doing so, we achieve fast operations, observe the quantum interference between the two Raman transitions and probe the GeV coherence ( $T_2^* = 224 \pm 14$  ns,  $T_2^H = 11.9 \pm 0.3$   $\mu$ s). Importantly, control via a double  $\Lambda$ -system is applicable to other color centers and particularly, the group-IV defects in diamond.

Realizing a quantum network will require developing light-matter interfaces consisting of coherent matter-qubits capable of emitting photons to perform long distance entangling gates [1–3]. Solid-state systems are particularly desirable in this role, as they are integrable into various micro- and nanostructures [4], while systems that operate in the optical domain cover larger distances than their microwave counterparts owing to low-loss fiber optics [5]. As optically-active solid-state systems with outstanding spin coherence times [6, 7], color centers are well suited to deployment as light-matter interfaces. Of the various color centers, group-IV split vacancy defects in diamond have attracted recent attention due to their excellent spin [8] and spectral properties [9]. These defects, possess an inversion symmetry derived insensitivity to electric fields that enables long coherence times [8] and lifetime limited optical emission [10], even when incorporated into an environment with significant electrical noise such as a nanophotonic cavity [11–13] – a key step in the efficient generation of long distance entanglement [1]. Additionally, short optical lifetimes on the order of nanoseconds and a high zero-phonon line emission (Debye-Waller factors exceeding  $\sim 70\%$  [14]) make group-IV defects promising candidates for high-efficiency spin-photon interfaces in a quantum network [15] and as a platform for microwave-to-optical transduction [16].

In this Letter, we focus on a single negatively-charged germanium vacancy (GeV). As a group-IV center with a ground-state spin-orbit coupling of  $\sim 165$  GHz [19], the GeV must be operated at temperatures  $\ll 300$  mK; in a dilution refrigerator, to *freeze-out* thermal excitation into a higher-energy orbital that would otherwise introduce decoherence [20]. At mK, cooling power is limited and fast electron spin operations may not be compatible with traditional magnetic resonance techniques due to power dissipation within the cryostat [21]. Weakly strained group-IV centres are particularly affected due

to exhibiting an almost non-existent magnetic coupling between the ground-state spin sub-levels [22, 23]. Yet, fast spin rotations are necessary for robust quantum information processing. Fortunately, optical control techniques offer a pathway to realizing these fast rotations by leveraging the orders of magnitude larger electric dipole moment of the optical transition over the spin magnetic moment.

Typically, optical control is realized via a Raman transition in a three-level  $\Lambda$ -system, here, formed from the ground state spin sub-levels and an optically excited state. This control scheme has been used to achieve incoherent control of the GeV [25], as well as coherent control of the silicon [20] and tin [26] vacancy defects. These centers approximate a  $\Lambda$ -system under certain experimental conditions and this enables such a control scheme. However, under other conditions, this approximation breaks down and the system is better described as a double  $\Lambda$ -system within which certain quantum interference effects may be observed. In this Letter, we demonstrate all-optical initialization, readout and coherent control of the GeV using the double  $\Lambda$ -system. By leveraging these interference effects, we achieve Rabi frequencies exceeding  $\sim 20$  MHz, with which we probe the coherence of the GeV in an off-axis magnetic field and at  $\sim 25$  mK.

The GeV may be viewed as consisting of a ground- and an excited-state spin-1/2 system [see Fig. 1(a)] [9, 18, 27, 28]. Following the standard nomenclature, we label the ground-state, spin-down eigenstate as  $|1\rangle$  and its excited-state counterpart  $|A\rangle$ , and likewise for the spin-up eigenstates,  $|2\rangle$  and  $|B\rangle$ . In a static magnetic field,  $B_0$ , the Zeeman effect lifts the ground-state spin degeneracy by  $\gamma_g B_0$  and its excited-state equivalent by  $\gamma_u B_0$ . Here,  $\gamma_{g,u} = \sqrt{\gamma_{\parallel,g,u}^2 \cos^2 \theta + \gamma_{\perp,g,u}^2 \sin^2 \theta}$ , and  $\gamma_{\perp}$  and  $\gamma_{\parallel}$  are the transverse and axial components of the g-tensor in the ground-state (excited-state) and  $\theta$  is the angle between the magnetic field and the GeV high-symmetry

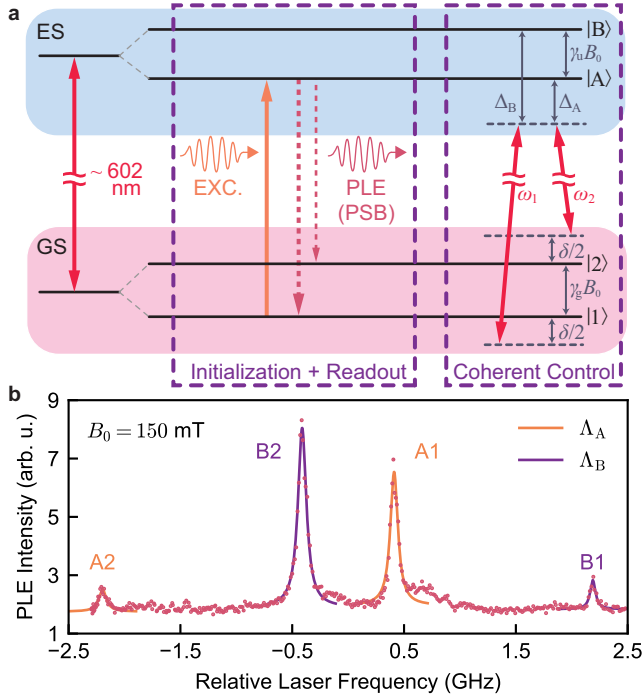


FIG. 1. (a) Level structure of the GeV with the initialization and readout, and the optical control schemes shown. In the initialization and readout scheme a resonant laser (EXC.) cycles the A1 transition with the resulting phonon side band (PSB) emission (PLE) collected. For optical control, two equal power (a consequence of the experimental setup [17, 18]) lasers with frequencies  $\omega_1$  and  $\omega_2$  are applied to drive the Raman transitions of  $\Lambda_A$  and  $\Lambda_B$ , simultaneously. (b) PLE spectrum of the GeV used in this work.

axis – in this case,  $\theta \sim 70.5^\circ$  while  $B_0 = 150$  mT. Owing to the strain dependence of  $\gamma_\perp$ , the Zeeman splitting and spin quantization axis differ between the ground- and excited-state, giving rise to two spin-conserving optical transitions that correspond to  $|1\rangle \leftrightarrow |A\rangle$  (A1) and  $|2\rangle \leftrightarrow |B\rangle$  (B2), and two weakly allowed spin-flipping transitions  $|2\rangle \leftrightarrow |A\rangle$  (A2) and  $|1\rangle \leftrightarrow |B\rangle$  (B1). All four transitions are spectrally resolvable as seen in Fig. 1(b).

For spin initialization and readout, we resonantly drive A1 as shown in Fig. 1(a) and 2(a). This pumps any population from  $|1\rangle$  into  $|2\rangle$  via optical relaxation through A2. As relaxation by A1 is favored, the transition will cycle and emit several photons before relaxation into  $|2\rangle$  quenches the emission. We observe this in Fig. 2(b), where we plot a histogram of the photoluminescence excitation (PLE) intensity during an A1 pulse and find that it decays exponentially with a decay time of  $\sim 42$  ns [29]. The PLE intensity at  $t_{A1} = 0$  ns is proportional to the population of  $|1\rangle$  prior to the A1 pulse,  $\mathcal{P}_{|1\rangle}$ , and therefore, by measuring this amplitude (referred to by “A1-READ PLE Int.” in later figures), we perform spin readout. By driving A1 until the emission is quenched, we have initialized the spin into  $|2\rangle$ .

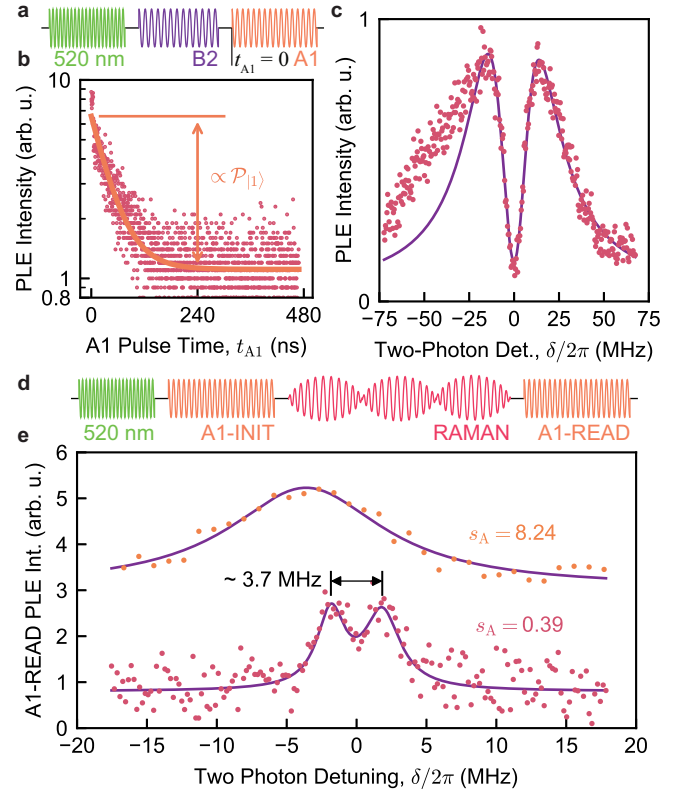


FIG. 2. (a) Pulse sequence used to measure the spin initialization into  $|2\rangle$  plotted in (b). Here, and throughout this Letter, the  $\sim 520$  nm laser pulse stabilizes the GeV charge configuration [24]. (b) A histogram of the photon arrival times, measured during the A1 spin-pumping pulse that transfers the population into  $|2\rangle$ . Here,  $\mathcal{P}_{|1\rangle}$  refers to the population in  $|1\rangle$  at  $t_{A1} = 0$  ns. (c) CPT spectrum performed with  $\Lambda_A$ . The data (red dots) is fit (purple curve) to the steady state of the CPT Lindblad superoperator [17]. (d) Pulse sequence used to measure the Raman spectrum presented in (e). (e) Raman spectra measured with a Raman power of  $s_A = 0.39$  (red dots) and  $s_A = 8.24$  (orange dots). The one-photon detunings were set to  $\Delta_A/2\pi \sim 790$  MHz and  $\Delta_B/2\pi \sim -970$  MHz.

To optically access the ground-state spin sub-levels, we first note that A1 and A2 as well as B2 and B1 form two  $\Lambda$ -systems that we label  $\Lambda_A$  and  $\Lambda_B$ . When driving both transitions of a  $\Lambda$ -system with two equal-powered lasers, we induce a transition between the ground-state spin sub-levels – here, referred to as the Raman drive – as shown in Fig. 1(a). In this particular system, the presence of two  $\Lambda$ -systems will result in the ground-state spin sub-levels being driven via both  $\Lambda$ -systems simultaneously. For the two Raman lasers with frequencies,  $\omega_1$  and  $\omega_2$  and the four optical transitions with frequencies,  $\omega_{A1}$ ,  $\omega_{A2}$ ,  $\omega_{B2}$  and  $\omega_{B1}$ , we define the one-photon detunings of the two  $\Lambda$ -systems as  $2\Delta_A = (\omega_1 + \omega_2) - (\omega_{A1} + \omega_{A2})$  and  $2\Delta_B = (\omega_1 + \omega_2) - (\omega_{B1} + \omega_{B2})$ , and the two-photon detuning as  $\delta = (\omega_1 - \omega_2) - \gamma_g B_0$ . These parameters hence define

the system Hamiltonian in the rotating frame as

$$\begin{aligned} \frac{H}{\hbar} = & \frac{\delta}{2}\sigma_z + \Delta_A |A\rangle\langle A| + \Delta_B |B\rangle\langle B| + \\ & \frac{1}{2}(\Omega_{A1} |1\rangle\langle A| + \Omega_{A2} |2\rangle\langle A| + \text{h.c.}) + \\ & \frac{1}{2}(\Omega_{B1} |1\rangle\langle B| + \Omega_{B2} |2\rangle\langle B| + \text{h.c.}), \end{aligned} \quad (1)$$

where  $\Omega_{A1}, \dots, \Omega_{B2}$  are the optical Rabi frequencies and  $\sigma_z = |2\rangle\langle 2| - |1\rangle\langle 1|$ . It should be noted that  $\Delta_A = \Delta_B + \delta + \gamma_u B_0$ .

We begin by performing coherent population trapping (CPT) [30, 31] on  $\Lambda_A$  to locate the Raman transition. To do so, we set  $\Delta_A = 0$  MHz, sweep  $\delta$  – by sweeping  $\omega_1$  and  $\omega_2$ , simultaneously – and record the steady state PLE intensity in a continuous wave measurement, the results of which are presented in Fig. 2(c). As  $\delta$  approaches 0 MHz, the Raman drive comes into resonance with A1 and A2 and excites the system. However, at the Raman resonance that occurs when  $\delta = 0$  MHz, excitation – and the resulting PLE emission – is prevented as the system steady state is a coherent superposition of  $|1\rangle$  and  $|2\rangle$  constituting a so-called dark state. This accounts for the *dip* in the spectrum at  $\delta = 0$  MHz as observed in Fig. 2(c) and is the signature of CPT. Power ripple of the Raman laser intensity as  $\delta$  is swept causes the experimental data (red dots) to deviate from the fit (purple line).

Prior to entering the dark state, coherent oscillations between  $|1\rangle$  and  $|2\rangle$  should occur. However, these decay very quickly, limited by the nanosecond optical decay time of the excited state, and cannot be observed under continuous excitation. These Raman-Rabi oscillations continue to occur even when non-zero one-photon detunings are used to reduce excitation into the excited state. Hence, we add a one-photon detuning and measure the resulting Raman spectrum using the pulse sequence in Fig. 2(d). Here, the spin is first initialized into  $|2\rangle$ , then coherently driven with a fixed duration Raman pulse of varying  $\delta$  and subsequently measured. The spectrum for one-photon detunings of  $\Delta_A/2\pi \sim 790$  MHz and  $\Delta_B/2\pi \sim -970$  MHz is plotted in Fig. 2(e), where we observe two peaks centered at  $\delta = 0$  MHz for low excitation powers (red dots). As the Raman spectrum provides greater resolution than CPT [18, 32], we are able to detect the hyperfine structure of a strongly coupled  $^{13}\text{C}$  nuclear spin [33], which introduces a  $\pm 1.9$  MHz nuclear state dependent shift to the Raman resonance [18] for the two  $^{13}\text{C}$  spin eigenstates. In addition to power broadening, higher Raman powers introduce a so-called AC Stark shift to the Raman resonance frequency [see Fig. 2(d) orange dots] that is a consequence of  $\Omega_{A1} \neq \Omega_{A2}$  and  $\Omega_{B2} \neq \Omega_{B1}$ .

We now directly measure Raman-Rabi oscillations by varying the Raman pulse duration while fixing  $\delta$  to be on resonance with the Raman transition [see Fig. 3(a)]. As shown in Fig. 3(b), the spin population in  $|1\rangle$  oscillates

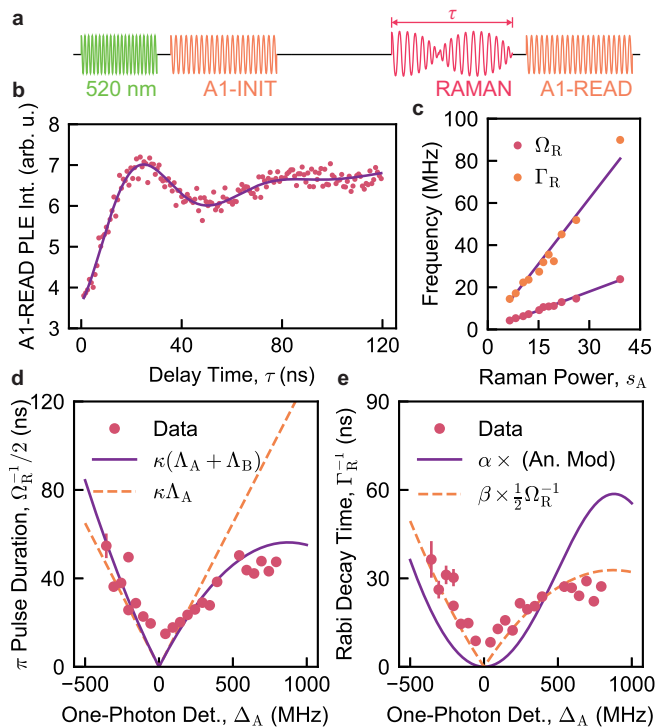


FIG. 3. (a) Pulse sequence used to measure Raman-Rabi oscillations. (b) Rabi oscillation measured with  $\Delta_A/2\pi \sim 240$  MHz and  $\Delta_B/2\pi \sim -1520$  MHz and with a Raman power of  $s_A \sim 17$ . The data (red dots) is fit to a decaying sinusoid (purple curve). (c) Rabi frequency ( $\Omega_R$ , red dots) and Rabi decay rate ( $\Gamma_R$ , orange dots) as measured for various Raman drive powers with the corresponding linear fits (purple lines). The one-photon detunings are the same as in (b). (d) The experimentally measured dependence of the  $\pi$ -pulse duration (red dots) on the one-photon detuning plotted alongside the values predicted by Eq. 2b (solid purple line, scaled by  $\kappa = 1/4$ ) and the values computed for when only  $\Lambda_A$  (the first term in Eq. 2b) is present (dashed orange line, scaled by  $\kappa = 1/4$ ). (e) The measured (red dots) one-photon detuning dependence of the Rabi decay time in addition to the theoretically predicted decay time were off-resonant scattering the dominant decoherence mechanism (purple line, scaled by  $\alpha = 1/350$ ) and the  $\pi$ -pulse duration calculated from Eq. 2b (orange dashed line, scaled by  $\beta = 0.19$ ). The data in (d) and (e) were measured with a Raman drive power of  $s_A \sim 18$ .

as the Raman-pulse duration is varied. The linear dependence in the Raman-Rabi frequency,  $\Omega_R$ , with respect to the Raman power [see Fig. 3(c)] confirms that these are Raman-Rabi oscillations. Also plotted in Fig. 3(c) is the Rabi decay rate,  $\Gamma_R$ , which is extracted from the decay of the oscillations and is proportional to Raman power. Therefore, this decay is induced by the drive and limits control.

Due to the specific strain configuration of our GeV, the system exhibits  $\gamma_u B_0 < \gamma_g B_0$  and  $\omega_{A2} < \omega_{B2} < \omega_{A1}$  [see Fig. 1(a)]. In other words,  $\Lambda_A$  and  $\Lambda_B$  cannot be separately driven. In a single  $\Lambda$ -system with optical

Rabi frequencies  $\Omega_1$  and  $\Omega_2$ , and one-photon detuning  $\Delta$ , the Raman-Rabi frequency is  $\frac{\Omega_1\Omega_2}{2\Delta}$ , when  $\Delta$  exceeds the natural linewidth,  $\Gamma$ , of the optical transitions [34]. In a multi- $\Lambda$ -system, the Raman-Rabi frequency is the sum of the Rabi frequencies over all  $\Lambda$ -systems. Here, this is [26],

$$\Omega_R = \frac{\Omega_{A1}\Omega_{A2}}{2\Delta_A} + \frac{\Omega_{B2}\Omega_{B1}}{2\Delta_B} \quad (2a)$$

$$\approx \frac{s_A\Gamma^2}{4\Delta_A} \frac{\sqrt{\eta_A^3}}{(1+\eta_A)^2} + e^{i\varphi} \frac{s_B\Gamma^2}{4\Delta_B} \frac{\sqrt{\eta_B^3}}{(1+\eta_B)^2}, \quad (2b)$$

where  $\varphi$  is the phase difference between  $\Omega_{A1}\Omega_{A2}$  and  $\Omega_{B2}\Omega_{B1}$ . Additionally,  $s_i = p^{\text{Raman}}/p_i^{\text{sat}}$ ,  $p_i^{\text{sat}}$  and  $\eta_i$  are the saturation parameter, saturation power and branching ratio for  $\Lambda_i$ , while  $p^{\text{Raman}}$  is the Raman excitation power. The measured saturation powers are  $p_A^{\text{sat}} = 211 \pm 13$  nW and  $p_B^{\text{sat}} = 203 \pm 9$  nW while the branching ratios for both  $\Lambda$ -systems is  $\eta_A \sim \eta_B \sim 3.1$  [17]. The step from Eq. 2a to Eq. 2b assumes that  $\Omega_{A2} \approx \Omega_{A1}/\sqrt{\eta_A}$  and likewise for  $\Lambda_B$ . It is unlikely that this approximation holds as  $\eta_{A,B}$  are extracted from the relaxation over all electric dipoles – oriented along the defect internal coordinate axes of  $x$ ,  $y$  and  $z$  [17] – while the Raman excitation is projected onto these dipoles based on laser polarization.

In Fig. 3(d), we plot the measured Rabi  $\pi$ -times for various one-photon detunings and observe a quadratic dependence with respect to  $\Delta_A$ . This dependence can be reproduced from Eq. 2b when  $\varphi = \pi$  is assumed and is a consequence of the interference between the two Raman transitions. The magnitude of the predicted values differs from those measured by a factor  $\kappa = 1/4$ , most likely due to the approximation made in translating from Eq. 2a to Eq. 2b. Nonetheless, the interference of the Raman transitions yields Rabi frequencies that are faster than those produced from a single  $\Lambda$ -system when  $\Delta_A$  is positive and  $\Delta_B$  is negative, or vice versa. The condition,  $\varphi = \pi$  arises when one of the optical Rabi paths – from A1 to B2 – is out of phase with the remaining three. This may occur when a GeV is operated in our experimental conditions [17].

We plot the corresponding Rabi decay times in Fig. 3(e) and observe a quadratic dependence with respect to  $\Delta_A$ . This is in contrast to the analytical model for decoherence via off-resonant scattering which predicts a decay that is slower and follows  $\approx \sum_{i \in \{A,B\}} \frac{s_i\Gamma^3}{8\Delta_i^2}$  [purple curve in Fig. 3(e)] [35]. Consequently, we rule out off-resonant scattering in addition to cross-talk [17] as the Raman-induced decoherence mechanism. Moreover, the Rabi decay time is proportional to the  $\pi$ -time which suggests that Raman excitation noise – likely from cryostat-induced vibration of the sample relative to the focal spot – is the dominant Rabi decay mechanism.

Finally, we investigate the spin coherence of the GeV. We begin by using the pulse sequence in Fig. 4(a) to

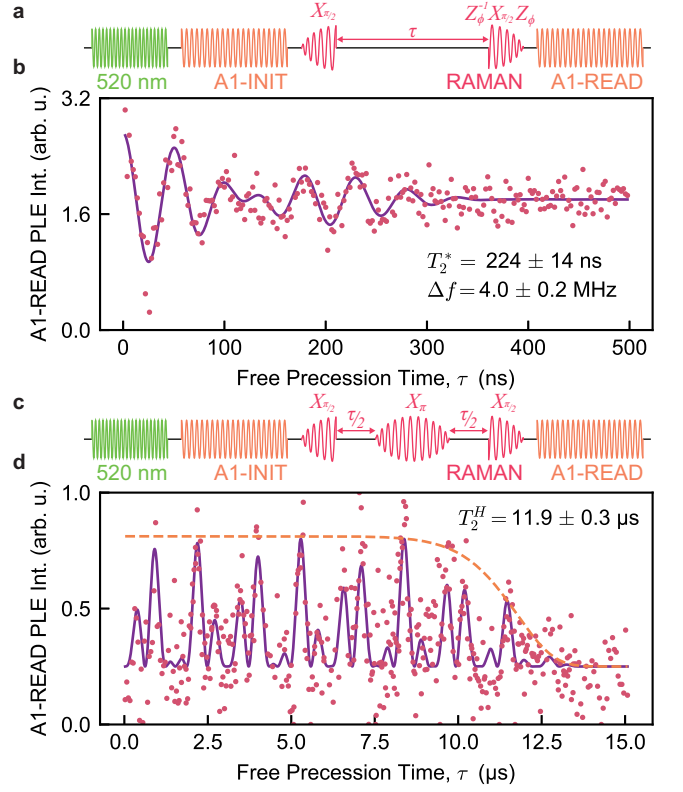


FIG. 4. Pulse sequences used to measure the free induction decay (a) and Hahn echo (c) coherence times. Here,  $X_\theta$  and  $Z_\theta$  refer to a qubit rotation of angle  $\theta$  around the  $x$ - or  $z$ -axes of the Bloch sphere. (b) Free induction decay. The data (red dots) is fit (purple line) to the sum of two decaying sinusoids with  $\Delta f$  denoting the difference in the two sinusoid frequencies. A linear  $\tau$ -dependent phase shift of  $\phi/\tau = 5$  MHz is applied to the second  $X_{\pi/2}$  pulse. The one-photon detuning is  $\Delta_A/2\pi \sim 790$  MHz ( $\Delta_B/2\pi \sim -970$  MHz) while the Raman power was  $s_A \sim 49$ . (d) Hahn echo. The data (red dots) is fit to an appropriate model (purple line) with the decay envelope (orange dashed line) shown. Here,  $\Delta_A/2\pi \sim 790$  MHz and  $\Delta_B/2\pi \sim -970$  MHz while  $s_A \sim 18$ .

measure the free induction decay [see Fig. 4(b)], where the free precession time,  $\tau$ , is increased. We observe a beating oscillation in the free induction decay with frequencies  $f_{\text{FID}}^{(\pm)} = f_\phi + f_{\text{Stark}} \pm \Delta f/2$ . Here,  $f_\phi = 5$  MHz is the  $\tau$ -dependent phase shift applied to the second  $\pi/2$ -pulse,  $f_{\text{Stark}} \sim 14$  MHz is the AC Stark shift during the Raman drive, and  $\Delta f$  is the hyperfine splitting from the aforementioned  $^{13}\text{C}$  spin. The Stark shift is only present during the  $\pi/2$ -pulses which are tuned to the Stark shifted resonance to ensure the proper rotation angle is achieved [comp. Fig. 2(e)]. Consequently, the qubit is detuned by the missing Stark shift during free precession. By fitting the free induction decay to the sum of two exponentially decaying sinusoids, we extract  $T_2^* = 224 \pm 14$  ns. This value is typical for group-IV defects in a largely misaligned magnetic field [8, 26]. We add a refocusing  $\pi$ -pulse to the sequence [see Fig. 4(c)]

to measure the Hahn echo coherence time and plot the results in Fig. 4(d). We observe coherence revivals that correspond to anisotropic hyperfine coupling to a proximal  $^{13}\text{C}$  nucleus. The Hahn echo signal is proportional to  $e^{-(\tau/T_2^H)^\beta} \sin^2(\kappa_-\tau) \sin^2(\kappa_+\tau)$  where,  $\kappa_\pm$  are the  $^{13}\text{C}$  nuclear magnetic resonance frequencies [36, 37]. From the fit, we extract  $T_2^H = 11.9 \pm 0.3 \mu\text{s}$ , as expected for a group-IV defect in a largely off-axis magnetic field [26].

Many optically active spin-1/2 systems can form a double  $\Lambda$ -system [38, 39] – most notably, the group-IV split vacancy defects where it is common for  $\gamma_u < \gamma_g$ . However, previous research regarding solid-state systems has almost exclusively focused on operating conditions that reduce these systems to single  $\Lambda$ -systems [20, 26, 40]. In contrast, we have realized coherent optical control of a solid-state spin through both possible Raman paths and observed the unique interference effects of the two Raman transitions. In doing so, we have achieved Raman-Rabi oscillations faster than would be possible in a single  $\Lambda$ -system without requiring higher Raman drive powers. This improvement in the Rabi frequency is significant as it enables fast, all-optical quantum gates – a requirement for robust quantum information processing – in the low cooling power environment of a dilution refrigerator. While we recognize that currently the GeV exhibits significant Raman induced decoherence, we note that this is not intrinsic to the physical system and improvements to the experimental setup would minimize this effect. Moreover, as the GeV optical response is strain and magnetic field dependent, the Raman transitions may be optimized to significantly improve the application of optical control techniques to the GeV or more broadly, the group-IV defects.

This work was funded by the Australian Research Council (grant no. CE170100012, CE200100010, FT220100053) and the Office of Naval Research Global (grant no. N62909-22-1-2028). We acknowledge the facilities, and the scientific and technical assistance provided by the NSW node of the Australian National Fabrication Facility (ANFF), and the Heavy Ion Accelerators (HIA) nodes at the Australian National University. ANFF and HIA are supported by the Australian Government through the National Collaborative Research Infrastructure Strategy (NCRIS) program. C. A. and A. L. acknowledge support from the University of New South Wales Scientia program.

---

\* Corresponding Author: [c.adambukulam@unsw.edu.au](mailto:c.adambukulam@unsw.edu.au)

† [a.laucht@unsw.edu.au](mailto:a.laucht@unsw.edu.au)

[1] H. J. Kimble, The quantum internet, *Nature* **453**, 1023 (2008).  
 [2] L.-M. Duan, M. D. Lukin, J. I. Cirac, and P. Zoller, Long-distance quantum communication with atomic ensembles and linear optics, *Nature* **414**, 413 (2001).

[3] S. D. Barrett and P. Kok, Efficient high-fidelity quantum computation using matter qubits and linear optics, *Phys. Rev. A* **71**, 060310 (2005).  
 [4] I. Aharonovich, D. Englund, and M. Toth, Solid-state single-photon emitters, *Nature Photonics* **10**, 631 (2016).  
 [5] N. J. Lambert, A. Rueda, F. Sedlmeir, and H. G. L. Schwefel, Coherent conversion between microwave and optical photons—an overview of physical implementations, *Advanced Quantum Technologies* **3**, 1900077 (2020).  
 [6] M. H. Abobeih, J. Cramer, M. A. Bakker, N. Kalb, M. Markham, D. J. Twitchen, and T. H. Taminiau, One-second coherence for a single electron spin coupled to a multi-qubit nuclear-spin environment, *Nature Communications* **9**, 2552 (2018).  
 [7] R. Nagy, M. Widmann, M. Niethammer, D. B. R. Dasari, I. Gerhardt, O. O. Soykal, M. Radulaski, T. Ohshima, J. Vučković, N. T. Son, I. G. Ivanov, S. E. Economou, C. Bonato, S.-Y. Lee, and J. Wrachtrup, Quantum properties of dichroic silicon vacancies in silicon carbide, *Phys. Rev. Appl.* **9**, 034022 (2018).  
 [8] D. D. Sukachev, A. Sipahigil, C. T. Nguyen, M. K. Bhaskar, R. E. Evans, F. Jelezko, and M. D. Lukin, Silicon-vacancy spin qubit in diamond: A quantum memory exceeding 10 ms with single-shot state readout, *Phys. Rev. Lett.* **119**, 223602 (2017).  
 [9] D. Chen, J. E. Fröch, S. Ru, H. Cai, N. Wang, G. Adamo, J. Scott, F. Li, N. Zheludev, I. Aharonovich, and W. Gao, Quantum interference of resonance fluorescence from germanium-vacancy color centers in diamond, *Nano Letters* **22**, 6306 (2022).  
 [10] C. Bradac, W. Gao, J. Forneris, M. E. Trusheim, and I. Aharonovich, Quantum nanophotonics with group IV defects in diamond, *Nature Communications* **10**, 5625 (2019).  
 [11] M. E. Trusheim, B. Pingault, N. H. Wan, M. Gündoğan, L. De Santis, R. Debroux, D. Gangloff, C. Purser, K. C. Chen, M. Walsh, J. J. Rose, J. N. Becker, B. Lienhard, E. Bersin, I. Paradeisano, G. Wang, D. Lyzwa, A. R.-P. Montblanch, G. Malladi, H. Bakhru, A. C. Ferrari, I. A. Walmsley, M. Atatüre, and D. Englund, Transform-limited photons from a coherent tin-vacancy spin in diamond, *Phys. Rev. Lett.* **124**, 023602 (2020).  
 [12] M. K. Bhaskar, D. D. Sukachev, A. Sipahigil, R. E. Evans, M. J. Burek, C. T. Nguyen, L. J. Rogers, P. Siyushev, M. H. Metsch, H. Park, F. Jelezko, M. Lončar, and M. D. Lukin, Quantum nonlinear optics with a germanium-vacancy color center in a nanoscale diamond waveguide, *Phys. Rev. Lett.* **118**, 223603 (2017).  
 [13] J. L. Zhang, K. G. Lagoudakis, Y.-K. Tzeng, C. Dory, M. Radulaski, Y. Kelaita, K. A. Fischer, S. Sun, Z.-X. Shen, N. A. Melosh, S. Chu, and J. Vučković, Complete coherent control of silicon vacancies in diamond nanopillars containing single defect centers, *Optica* **4**, 1317 (2017).  
 [14] E. Neu, D. Steinmetz, J. Riedrich-Möller, S. Gsell, M. Fischer, M. Schreck, and C. Becher, Single photon emission from silicon-vacancy colour centres in chemical vapour deposition nano-diamonds on iridium, *New Journal of Physics* **13**, 025012 (2011).  
 [15] C. M. Knaut, A. Suleymanzade, Y.-C. Wei, D. R. Assumpcao, P.-J. Stas, Y. Q. Huan, B. Machielse, E. N. Knall, M. Sutula, G. Baranes, N. Sinclair, C. De-

- Enknamkul, D. S. Levonian, M. K. Bhaskar, H. Park, M. Lončar, and M. D. Lukin, Entanglement of nanophotonic quantum memory nodes in a telecommunication network (2023), [arXiv:2310.01316 \[quant-ph\]](#).
- [16] T. Neuman, M. Eichenfield, M. E. Trusheim, L. Hackett, P. Narang, and D. Englund, A phononic interface between a superconducting quantum processor and quantum networked spin memories, *npj Quantum Information* **7**, 121 (2021).
- [17] See Supplemental Material at [link to be provided by publisher], which includes Refs. 41 and 42, for details regarding the sample preparation and experimental setup, characterization of the defect, modelling CPT and confirmation of the presence of a  $^{13}\text{C}$  spin.
- [18] C. Adambukulam, B. C. Johnson, A. Morello, and A. Laucht, Hyperfine spectroscopy and fast, all-optical arbitrary state initialization and readout of a single, ten-level  $^{73}\text{Ge}$  vacancy nuclear spin qudit (2023), [arXiv:2309.04126 \[cond-mat.mes-hall\]](#).
- [19] S. Maity, L. Shao, Y.-I. Sohn, S. Meesala, B. Machielse, E. Bielejec, M. Markham, and M. Lončar, Spectral alignment of single-photon emitters in diamond using strain gradient, *Phys. Rev. Appl.* **10**, 024050 (2018).
- [20] J. N. Becker, B. Pingault, D. Groß, M. Gündoğan, N. Kukharchyk, M. Markham, A. Edmonds, M. Atatüre, P. Bushev, and C. Becher, All-optical control of the silicon-vacancy spin in diamond at millikelvin temperatures, *Phys. Rev. Lett.* **120**, 053603 (2018).
- [21] H. H. Vallabhapurapu, J. P. Slack-Smith, V. K. Sewani, C. Adambukulam, A. Morello, J. J. Pla, and A. Laucht, Fast coherent control of a nitrogen-vacancy-center spin ensemble using a  $\text{KTaO}_3$  dielectric resonator at cryogenic temperatures, *Phys. Rev. Appl.* **16**, 044051 (2021).
- [22] E. I. Rosenthal, C. P. Anderson, H. C. Kleidermacher, A. J. Stein, H. Lee, J. Grzesik, G. Scuri, A. E. Rugar, D. Riedel, S. Aghaeimeibodi, G. H. Ahn, K. Van Gasse, and J. Vučković, Microwave spin control of a tin-vacancy qubit in diamond, *Phys. Rev. X* **13**, 031022 (2023).
- [23] S. Meesala, Y.-I. Sohn, B. Pingault, L. Shao, H. A. Atikian, J. Holzgrafe, M. Gündoğan, C. Stavrakas, A. Sipahigil, C. Chia, R. Evans, M. J. Burek, M. Zhang, L. Wu, J. L. Pacheco, J. Abraham, E. Bielejec, M. D. Lukin, M. Atatüre, and M. Lončar, Strain engineering of the silicon-vacancy center in diamond, *Phys. Rev. B* **97**, 205444 (2018).
- [24] D. Chen, Z. Mu, Y. Zhou, J. E. Fröch, A. Rasmit, C. Diederichs, N. Zheludev, I. Aharonovich, and W.-b. Gao, Optical gating of resonance fluorescence from a single germanium vacancy color center in diamond, *Phys. Rev. Lett.* **123**, 033602 (2019).
- [25] P. Siyushev, M. H. Metsch, A. Ijaz, J. M. Binder, M. K. Bhaskar, D. D. Sukachev, A. Sipahigil, R. E. Evans, C. T. Nguyen, M. D. Lukin, P. R. Hemmer, Y. N. Palyanov, I. N. Kupriyanov, Y. M. Borzdov, L. J. Rogers, and F. Jelezko, Optical and microwave control of germanium-vacancy center spins in diamond, *Phys. Rev. B* **96**, 081201 (2017).
- [26] R. Debroux, C. P. Michaels, C. M. Purser, N. Wan, M. E. Trusheim, J. Arjona Martínez, R. A. Parker, A. M. Stramma, K. C. Chen, L. de Santis, E. M. Alexeev, A. C. Ferrari, D. Englund, D. A. Gangloff, and M. Atatüre, Quantum control of the tin-vacancy spin qubit in diamond, *Phys. Rev. X* **11**, 041041 (2021).
- [27] C. Hepp, T. Müller, V. Waselowski, J. N. Becker, B. Pingault, H. Sternschulte, D. Steinmüller-Nethl, A. Gali, J. R. Maze, M. Atatüre, *et al.*, Electronic structure of the silicon vacancy color center in diamond, *Physical Review Letters* **112**, 036405 (2014).
- [28] R. A. Parker, J. Arjona Martínez, K. C. Chen, A. M. Stramma, I. B. Harris, C. P. Michaels, M. E. Trusheim, M. Hayhurst Appel, C. M. Purser, W. G. Roth, D. Englund, and M. Atatüre, A diamond nanophotonic interface with an optically accessible deterministic electronuclear spin register, *Nature Photonics* **10.1038/s41566-023-01332-8** (2023).
- [29] Before applying the A1 pulse, the system was prepared in the  $|1\rangle$  state using a B2 pulse, as indicated in Fig. 2(a).
- [30] B. Pingault, J. N. Becker, C. H. H. Schulte, C. Arend, C. Hepp, T. Godde, A. I. Tartakovskii, M. Markham, C. Becher, and M. Atatüre, All-optical formation of coherent dark states of silicon-vacancy spins in diamond, *Phys. Rev. Lett.* **113**, 263601 (2014).
- [31] X. Xu, S. Bo, P. R. Berman, D. G. Steel, A. S. Bracker, D. Gammon, and L. Sham, Coherent population trapping of an electron spin in a single negatively charged quantum dot, *Nature Physics* **4**, 692 (2008).
- [32] B. D. Agap'ev, M. B. Gornyi, B. Matisov, and Y. V. Rozhdestvenskiĭ, Coherent population trapping in quantum systems, *Physics-Uspekhi* **36**, 763 (1993).
- [33] A. Karim, H. H. Vallabhapurapu, C. Adambukulam, A. Laucht, S. P. Russo, and A. Peruzzo, All-electron *ab-initio* hyperfine coupling of Si-, Ge- and Sn-vacancy defects in diamond (2023), [arXiv:2309.13913 \[cond-mat.mes-hall\]](#).
- [34] D. F. James and J. Jerke, Effective Hamiltonian theory and its applications in quantum information, *Canadian Journal of Physics* **85**, 625 (2007).
- [35] C. J. Foot, *Atomic Physics* (Oxford University Press, New York, USA, 2005).
- [36] B. D. Wood, G. A. Stimpson, J. E. March, Y. N. D. Lekhai, C. J. Stephen, B. L. Green, A. C. Frangeskou, L. Ginés, S. Mandal, O. A. Williams, and G. W. Morley, Long spin coherence times of nitrogen vacancy centers in milled nanodiamonds, *Phys. Rev. B* **105**, 205401 (2022).
- [37] L. G. Rowan, E. L. Hahn, and W. B. Mims, Electron-spin-echo envelope modulation, *Phys. Rev.* **137**, A61 (1965).
- [38] K. G. Lagoudakis, K. A. Fischer, T. Sarmiento, P. L. McMahon, M. Radulaski, J. L. Zhang, Y. Kelaita, C. Dory, K. Müller, and J. Vučković, Observation of mollow triplets with tunable interactions in double lambda systems of individual hole spins, *Phys. Rev. Lett.* **118**, 013602 (2017).
- [39] X. Xu, S. Shen, and Y. Xiao, Tuning the phase sensitivity of a double-lambda system with a static magnetic field, *Opt. Express* **21**, 11705 (2013).
- [40] J. N. Becker, J. Görlitz, C. Arend, M. Markham, and C. Becher, Ultrafast all-optical coherent control of single silicon vacancy colour centres in diamond, *Nature Communications* **7**, 13512 (2016).
- [41] D. Manzano, A short introduction to the Lindblad master equation, *AIP Advances* **10**, 025106 (2020).
- [42] C. J. Hepp, *Electronic Structure of the Silicon Vacancy Color Center in Diamond*, Ph.D. thesis, Universität des Saarlandes (2014).